



The computational analysis of shallow depth tabular mining problems

by J.A.L. Napier* and D.F. Malan†

Synopsis

The evaluation of stress distributions and deformations in the vicinity of tabular mine layouts has been carried out routinely for many years using the displacement discontinuity boundary element method (DDM). In this approach, mine layouts are approximated as irregular shaped planar cracks (or slits) where the 'width' of the crack, corresponding to the excavation height, is assumed to be negligible compared to the in-plane, lateral dimensions. Early implementations of this approach have employed square element tessellations with constant displacement discontinuity component values. This is generally restrictive when considering the analysis of irregular pillar layouts or the intersection of fault planes with excavations. This paper describes a general revision of this approach in which triangular or quadrilateral element shapes are introduced in conjunction with higher order variations of the displacement discontinuity shape functions. This facilitates an accurate evaluation of detailed stress and displacement components close to excavation surfaces and allows the investigation of local damage and failure behaviour associated with particular geological structures such as weak parting bands or weak layers. A method to embed these features in an efficient and accurate multi-level solution scheme is described. This formulation can be extended to allow the analysis of shallow-depth pillar layout problems, facilitating the assessment of the interactive response and stability of shallow depth pillar layouts. A simple deformation model is introduced to facilitate the assessment of pillar failure and bursting potential in shallow mine layouts. The computational techniques described here have been implemented in a computer code called TEXAN (Tabular EXcavation ANALyser) and are illustrated by the simulation of a particular multiple reef pillar mining problem in a shallow depth platinum mine.

Introduction

The now classical method used for the computational analysis of stress distributions in the vicinity of coal, gold and platinum mine tabular excavations is the displacement discontinuity boundary element method (DDM). The use of this technique in the design of tabular excavations dates almost from the general availability of digital computer facilities to the mining industry, over fifty years ago. In the South African context, this approach was pioneered by Salamon in the early 1960s and was summarized in his

seminal papers published in the South African Institute of Mining and Metallurgy *Journal* (see Salamon, 1963, 1964a, 1964b, 1965). Further interest in the method has been presented in several journal and conference papers (see, for example, Ryder and Officer, 1964, Plewman *et al.*, 1969, Crouch, 1973, Brady and Bray, 1978, Moris and Oravec, 1985). An entirely innovative application of the then somewhat unfamiliar technique of Fast Fourier transforms (FFT) was developed by Stuart in a novel but unpublished research thesis (Stuart, 1979). This approach exploits the implicit convolution structure of the influence coefficients in formulating an efficient, single-reef tabular excavation solution technique. This has subsequently been explained in greater detail by Peirce *et al.*, 1992 and applied to good effect by Spottiswoode, 2004.

Implementation of the DDM has appeared internationally in a number of software tools such as MULSIM (Zipf, 1992) and in software suites developed by Crouch (see, for example, Crouch, 1973). Further extensions and applications have been detailed by Yacoub and Curran, 1999, Vijayakumar *et al.*, 2000 and Wiles, 2006. Local software tools developed in South Africa have been embodied in the MINSIM codes (Deist *et al.*, 1972, Ryder and Napier, 1985 and Napier and Stephansen, 1987).

This partial list of applications of the DDM is not intended to be exhaustive but does serve to illustrate the manifest utility of the DDM in tabular excavation analysis and design. The main motivation for the current paper is to emphasize a number of novel extensions to the basic method that have not been

* CSIR Fellow and School of Computational and Applied Mathematics, University of the Witwatersrand, Johannesburg.

† Groundwork Consulting (Pty) Ltd, Johannesburg.

© The Southern African Institute of Mining and Metallurgy, 2007. SA ISSN 0038-223X/3.00 + 0.00. Paper received Jun. 2007; revised paper received Oct. 2007.

The computational analysis of shallow depth tabular mining problems

implemented previously. The study is further impelled by the continuing need to analyse practical tabular mining problems in South Africa with particular emphasis on shallow depth pillar design and efficient fault slip simulations. Thus, the DDM provides an ideal practical computational utility for large-scale tabular excavation design problems but is also deserving of ongoing research in relation to a number of fundamental numerical issues.

The paper outline is as follows: The status of shape function choice in implementing the DDM is first discussed, followed by a review of the computational technique known colloquially as 'lumping' and by an outline of a fresh approach that has been developed to allow the efficient computation of shallow depth, high order influence functions. This basic discussion is followed by the development of a simple model of crush and yield pillar failure and by an illustrative application of this approach to the problem of a multiple reef platinum mine pillar layout analysis. Some important and achievable extensions to the developed analysis strategy are suggested as concluding remarks. Two Appendices are included for reference purposes to provide a simplified derivation of the half-space (shallow depth) displacement discontinuity influence function kernels and to provide the details of the high order shape function formulation employed in the paper.

Element shapes and displacement discontinuity shape functions

The detailed formulation of the displacement discontinuity method will not be discussed in this paper (see, for example, Jaswon and Symm, 1977, Crouch and Starfield, 1983). The main point to note is that the width (mining height) of the excavation is neglected in comparison to the lateral dimensions. This serves as a useful approximation, except very close to the excavation edges. Even in this case, it may be shown that the use of appropriate 'soft seam' models (Crouch and Starfield, 1983) allows for good approximations to the actual distribution of stress near the excavation surface. Naturally, it is important to assess when such an approximation should be suspended and replaced by an explicit representation of inelastic face deformations and fracture processes (see, for example, Napier and Hildyard, 1992). The basic integral equation relationships (see Appendix A) allow stress and displacement components to be computed at any point in the region of interest in terms of the distribution of displacement discontinuity values on all significant surfaces representing both tabular excavations and fault planes. The displacement discontinuity vector components $D_i(Q)$ at any point, Q , of one of these surfaces are defined to be the difference between the displacement vectors $u_i^+(Q)$ and $u_i^-(Q)$ on each side of the surface at point Q . The superscripts '+' and '-' designate the two sides of the surface with respect to the surface normal vector, $n_i(Q)$, defined at point Q (see Appendix A). The discontinuity distribution $D_i(Q)$ at all points Q is, in general, not known and the essential task is to solve the defining integral equations for this distribution in order to satisfy specified boundary conditions on the interacting excavation and fault surfaces.

Several approaches may be followed to determine the unknown displacement discontinuity distribution, which generally does not admit an analytical solution. The most direct approach, discussed in this paper, is to split the surface into a number of sub-regions (termed elements) and to assign a particular, simplified functional form to the displacement discontinuity distribution within each element.

In the earliest applications of the DDM to mine layout problems this function was assumed simply to be a constant within each element and the element shape was assumed to be square. Computer codes such as MINSIM-D (Ryder and Napier, 1985) are based on this strategy. In many cases, this approach is extremely effective but does exhibit a number of shortcomings.

One of the shortcomings is the empirical observation that the magnitudes of the solved displacement discontinuity values are affected by the imposed element mesh or grid size. This has been discussed and addressed by Ryder and Napier, 1985, who proposed corrective measures to ensure that the displacement discontinuity distribution can be more accurately determined by defining the concept of 'partially mined elements' and arranging that excavation outlines should be shifted by the 'quarter grid correction' (see Ryder and Napier, 1985). This strategy allows for accurate far-field stress distributions to be computed that are element size independent (mesh objective). A major shortcoming of the quarter grid shift and partially mined element strategy is that it becomes difficult to estimate average pillar stresses as pillar outlines are now 'blurred' or, in extreme cases, completely obliterated.

It is apparent, as well, that the exclusive use of square element shapes imposes geometric restrictions on the general and flexible representation of complicated mine layout patterns. One of the main strengths of the DDM is the ability to represent general layout patterns and it is unnecessary to compromise this feature. This is most obviously addressed by introducing triangular or quadrilateral-shaped elements, as illustrated in Figures 1a and 1b respectively. General polygonal shapes may obviously be built entirely from triangular elements but it is useful to allow the quadrilateral shape as well for particular applications (including the study of idealized layout patterns comprising square or rectangular elements).

The functional variation for each component of the displacement discontinuity (DD) vector, in each element, is assumed to have a simple polynomial expansion of the form

$$V(x, y) = \sum_{0 \leq p+q \leq n} c_{pq} x^p y^q \quad [1]$$

where n is the expansion order, p and q are integers and x and y are local variables in the element plane. In the special case of constant variation DD values, the expansion order is $n = 0$ and $V(x, y) = C$. The expansion coefficients c_{pq} are determined by evaluating the DD vector at selected collocation points within each element, as shown in Figure 1. The choice of internal, rather than shared vertex (Yacoub and Curran, 1999, Vijayakumar *et al.*, 2000) or shared edge, collocation points has been made to allow for the routine treatment of intersecting, angled planes such as at a fault-reef intersection

The computational analysis of shallow depth tabular mining problems

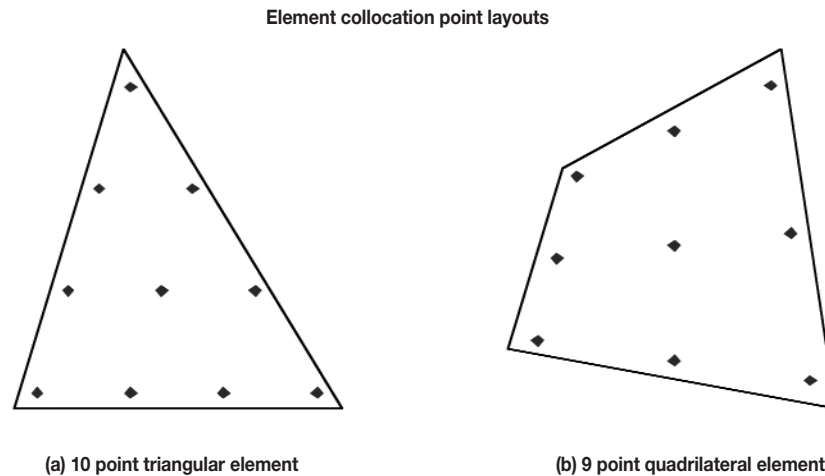


Figure 1—Collocation point distribution in illustrative triangular and quadrilateral shaped elements

line or the explicit modeling of features such as a key block with bounding plane surfaces. A simple procedure that may be followed to assemble the shape function expansions that are associated with each element collocation point is outlined in Appendix B.

As an illustration of the properties of higher order cubic variation elements having 10 internal collocation points per element (polynomial order, $n = 3$), consider the case of a circular excavation (or circular crack) in an infinite medium with a uniform stress field normal to the plane of the excavation. A tessellation of the element surface into 228 triangular (Delaunay) elements is shown in Figure 2. The nominal radius of the excavation is 10 m. Define the average element size g to be

$$g = \sqrt{A/N} \quad [2]$$

where A is the total excavation area and N is the total number of elements. Hence, in Figure 2, $g \sim 1.17$ m. The analytical solution for the normal component, D_z , of the elastic convergence of a circular opening centred on the origin in the x - y plane (Sneddon, 1951) in a remote stress field, Q_z , is given by the expression

$$D_z(x, y) = \frac{-4(1-\nu)Q_z}{\pi G} (R^2 - x^2 - y^2)^{1/2} \quad [3]$$

where ν is Poisson's ratio, G is the shear modulus, R is the excavation radius and x, y are the coordinates of any point on the nominal excavation surface. Note that $D_z = u_z^- - u_z^+$ and that Q_z is assumed to be negative when compressive. With this convention, D_z assumes positive values in a compressive stress field. Assuming that $G = 30\,000$ MPa, $\nu = 0.2$ and $Q_z = -50$ MPa, it is found that $D_z(0,0) = 16.9765$ mm. Squaring both sides of Equation [3] yields the relationship

$$D_z^2(r) = D_z^2(0)(R^2 - r^2) \quad [4]$$

where $D_z(0) = -4(1-\nu)Q_z/\pi G$ and $r^2 = x^2 + y^2$. A plot of D_z^2 vs. r^2 , for all 228 collocation points associated with the triangular tessellation of Figure 2, is shown in Figure 3. The

values are compared to the analytic solution given by Equation [4] over the edge region where $80 \leq r^2 \leq 100$ and can be seen to follow the analytic solution closely. Equivalently, good agreement is found in the inner region $0 \leq r^2 \leq 80$. The question arises whether this represents an improvement over the use of constant elements having an equivalent number of collocation points. The analysis was repeated using a finer triangular tessellation comprising 2306 triangles covering the circular opening. The corresponding plot of D_z^2 vs r^2 is also shown in Figure 3 (square points), indicating that the constant element solution has a significant bias and greater scatter relative to the higher order cubic element solution. It may also be noted that in the present analysis and code implementation, the computation run time for the higher order cubic element analysis was about 18 per cent of the run time for the constant element analysis—a more than fivefold improvement for approximately the same number of degrees of freedom (2280 collocation points for the higher order cubic element analysis vs. 2306 collocation points for the constant element analysis).

The higher order elements also yield accurate field point values close to the excavation surface. The analytic expression for the total stress component, σ_{zz} , at a position $Z = z/R$ above the centre of the circular opening, can be derived by substituting Equation [3] for the DD variation into Equations [A18] and [A17]. Performing the necessary integrations, it can be shown that

$$\sigma_{zz}/Q_z = \frac{2}{\pi} \left[\frac{Z}{1+Z^2} - \frac{2Z}{(1+Z^2)^2} + \tan^{-1} Z \right] \quad [5]$$

Figure 4 shows a comparison of the analytic values of σ_{zz}/Q_z according to Equation [5] compared to the numerical values with constant elements (number of collocation points equal to 228 and 2306 respectively) and the values determined using the higher order cubic elements. It is again clear that the higher order elements perform better than the constant elements. It is apparent, as well, that the field point values for the constant elements are not seriously in error once the field point is far enough from the excavation

The computational analysis of shallow depth tabular mining problems

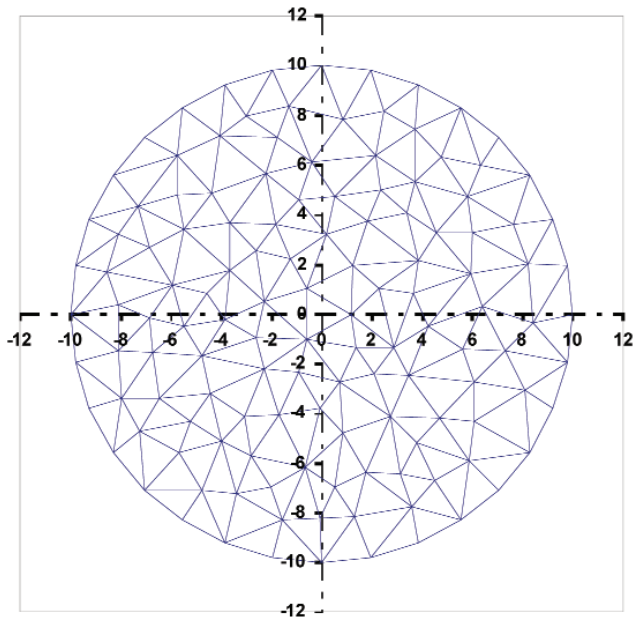


Figure 2—Circular excavation shape covered with 228 triangular elements

surface. For the case where 228 triangles are used, the average element size is about 1.17 m and for the finer tessellation with 2 306 triangles, the average element size is about 0.37 m. From Figure 4, it can then be inferred that, for this example, if the distance to the excavation surface exceeds twice the element size (i.e. $z/R \sim 0.234$ for 228 constant element triangles and $z/R \sim 0.074$ for 2 306 constant element triangles) then the error in the value of the σ_{zz} stress component is relatively small, although there is a clear asymptotic bias in the stress values as z/R increases. However, in the case where the higher order cubic elements are used, the bias is reduced significantly (see Figure 4) and the near-excitation stress variation is represented much more accurately at distances off the element surface that are much less than the element size.

It must be noted that in constructing the different cases shown in Figure 4, the central collocation point at the central triangle centroid is arranged to coincide with the origin of the circular tabular opening (see Figure 2) and the numerical field points are not computed at or close to an element boundary. It is found, however, that the use of the cubic variation shape functions also reduces the expected 'spike' in

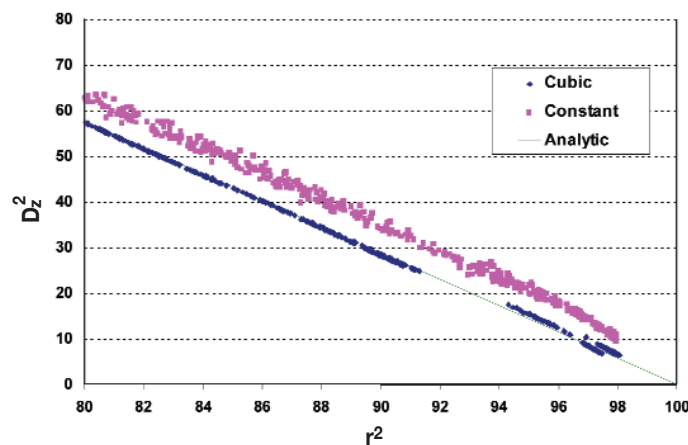


Figure 3—Comparison of normal closure component error near the edge of a circular opening when using cubic (2 280 collocation points) or constant (2 306 collocation points) element shape variations. Values of the closure component squared are plotted against the square of the radial position of each collocation point

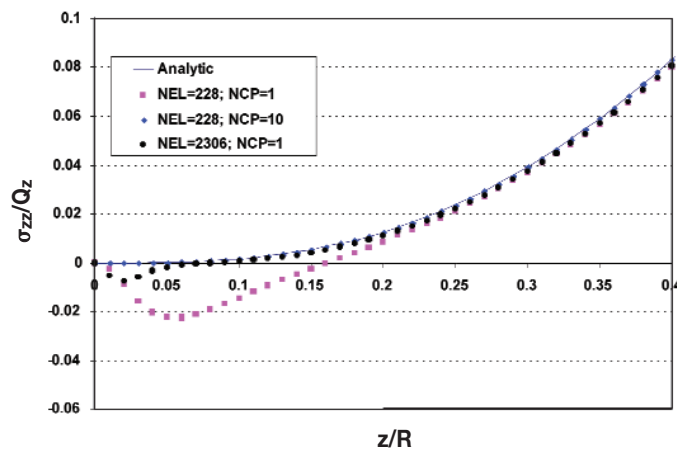


Figure 4. Comparison of the analytical solution for the stress component along the z-axis normal to the opening, to the values computed using constant elements and higher order cubic elements. (The acronyms NEL and NCP in the figure legend refer to the total number of elements covering the circular region and the number of collocation points per element respectively.)

The computational analysis of shallow depth tabular mining problems

field point values that might arise close to an element boundary. This singular behaviour can be expected to occur when an internal element collocation point strategy, such as in Figure 1, is used and where, consequently, the continuity and slope of the discontinuity vector components, $D_i(Q)$, are not maintained for points Q on adjacent sides of each element boundary.

Figure 5 is a plot of the induced horizontal (surface parallel) stress component evaluated at a distance of 0.1 m from the surface of the excavation using 2 306 constant and 228 cubic variation elements respectively. In the case of the constant element stress plot (points marked as squares in Figure 5), the distance of the field point line relative to the element size is approximately equal to 0.27 and clearly manifests the effects of the local, spurious stress singularities that arise near element boundaries. In the case of the cubic variation elements, the distance of the field point line relative to the element size is about 0.085 but even at this proximity does not exhibit significant stress perturbations. Clearly, the higher order elements provide significantly increased access to field points that are relatively close to the excavation surface. This is a particularly important attribute when analysing shallow pillar mining problems where inelastic deformations in the rock mass are small and where back-break or beam failure mechanisms may be important. On the other hand, it is also important to note that field points located outside the excavation region and close to or on the excavation plane are reasonably well estimated when using constant elements as may be seen in Figure 5 in the regions where $|x| > 10$.

Efficient solution strategy

Large-scale problems involving multiple reef excavations and fault planes may comprise many thousands of collocation

points (100 000 or more). In these cases, it is no longer feasible to apply a direct iterative method in which the computational cost per iteration will be proportional to the square of the number of elements. One of the early innovations introduced in the development of the MINSIM programs (Deist *et al.*, 1972) was the introduction of a computational technique termed 'lumping'. This technique can be recognized as a hierarchical tree method (see, for example, Pflanzner and Gibbon, 1996) and provides a very useful method to reduce the computational cost in large-scale problems. The technique is particularly suited to problems (such as in tabular mining) where the element tessellations are constrained to fall on flat planes. (In fact, the treatment of non-planar excavations or faults may be analysed, as well, by the tree approach provided the excavation or fault surfaces have sufficiently small curvatures relative to their spatial extent. This possibility will not be considered in the present paper).

Fast Fourier (FFT) and fast multipole methods (Stuart, 1979, Peirce *et al.*, 1992, Spottiswoode, 2004, Peirce and Napier, 1995) provide a competing approach to the multi-level tree analysis technique. The implementation of the FFT/multipole method is generally restricted to cases of single infinite depth excavation horizons or multiple, surface-parallel excavations that are tessellated with regular square or rectangular elements. This approach becomes awkward and inefficient when considering arbitrarily orientated multiple reef and fault planes, intersecting fault-reef or fault-fault geometries and shallow depth problems. Multipole expansions combined with FFT convolutions in three-dimensional space are also cumbersome when considering displacement discontinuity influence functions.

Early applications of the lumping approach to the solution of tabular mining problems assumed square elements and defined macro-sized element clusters comprising 2×2 , 4×4

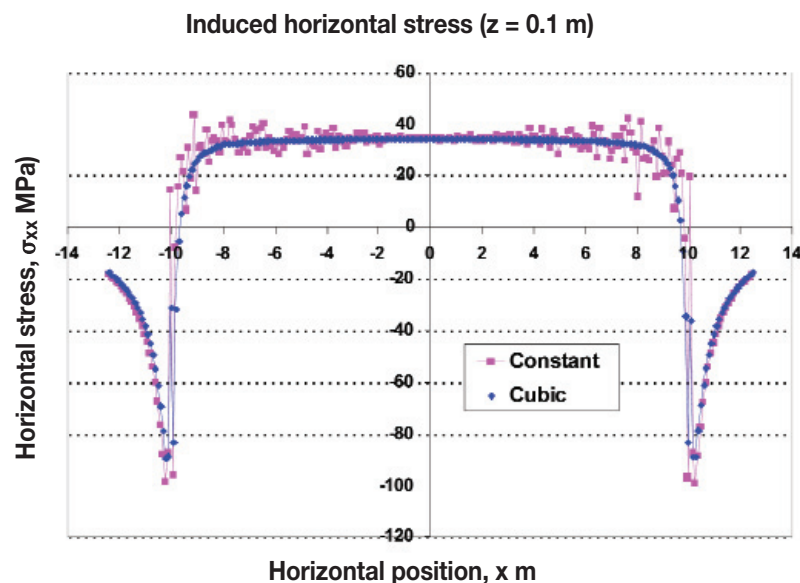


Figure 5—Comparison of horizontal stress field point values at a distance of 0.1 m above the plane of the circular opening when using constant or cubic variation triangular elements

The computational analysis of shallow depth tabular mining problems

etc. element groups or cells (see, for example, Napier and Stephansen, 1987). Since the macro-elements (or 'lumps') are geometrically self-similar to the finest level elements, it is possible to compute influence values using the same influence coefficients as at the finest level. (A modification of this scheme was introduced by Ryder and Napier, 1985, to transmit averaged rather than point influence values to receiving lumps). A restriction is imposed that, at any given hierarchical level, influence values transmitted only between receiving and sending lump cells are not less than a specified minimum distance apart and are not further than a maximum distance apart. These lump influence boundaries are defined by an 'inner ring' region that is an integer multiple, s , of the receiving lump cell size and is centred on the receiving lump cell and an 'outer ring' that is the same multiple, s , of the parent lump cell size and centred on the parent lump.

A fragment of such a lump grid arrangement is shown in Figure 6 where the specified lump gap multiple is $s = 2$. Parts of the inner ring and outer ring boundaries are shown with respect to the receiving lump with size G and the corresponding parent lump having size $2G$. (i.e. each 'parent' lump contains four 'daughter' lumps as depicted in Figure 6). In previous implementations of this lumping strategy (such as in the MINSIM-D computer code developed by Ryder and Napier, 1987), constant influence values are then computed at the centre of each receiving lump and accumulated without further interpolation at the finest element level. The relatively crude nature of this scheme necessitates that the lump gap multiple, s , should not be less than 3 and can result in visible 'ripples' appearing in field point plots.

A revised scheme is proposed in this paper in order to treat triangular and quadrilateral shaped elements that may have higher order variation displacement discontinuity shape functions and which may be evaluated using shallow depth (half-space) influence functions. In this scheme, the square-cell lump grid structure, as depicted in Figure 6, is maintained but is not tied to the element tessellation layout. The lumping interpolation grid is superimposed on each reef and fault plane and the finest lump level (designated as level 1) cell

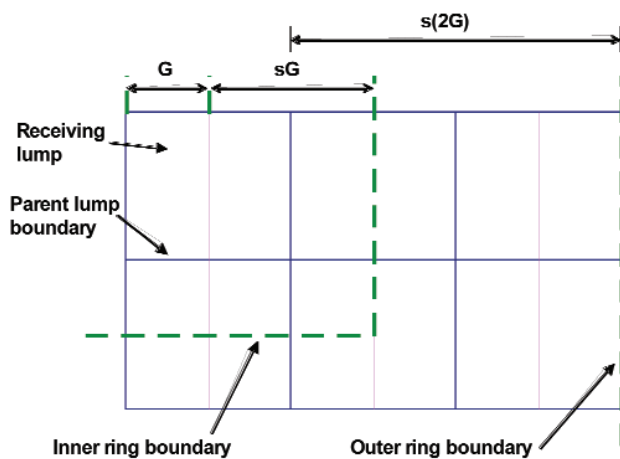


Figure 6—Schematic lump grid layout illustrating the inner and outer ring influence boundaries for a receiving lump of size G with the lump gap parameter, $s = 2$

size is defined to be G on all planes. The lump size at level L is then given by

$$G_L = 2^{L-1} G \quad [6]$$

Each element is then assigned to an appropriate lump cell i_L, j_L at level L using the relationships

$$i_L = \lfloor x_c / G_L \rfloor \text{ and } j_L = \lfloor y_c / G_L \rfloor \quad [7]$$

where $\lfloor a \rfloor$ designates the largest integer value not exceeding a and x_c, y_c are the coordinates of the element centroid in the local coordinate system of the element plane. The area of lump cell i_L, j_L covers all points x, y over the ranges $i_L G_L \leq x < (i_L + 1) G_L$ and $j_L G_L \leq y < (j_L + 1) G_L$. It is apparent that the boundaries of certain elements may intersect and extend beyond the boundary of the assigned element lump cell i_L, j_L . In order to address this possibility and to improve the overall accuracy of the lumping scheme an interpolation grid is introduced on each receiving lump cell and comprises 9 or 16 uniformly spaced points allowing for a bi-quadratic or bi-cubic interpolation of received influence values to the individual collocation points of all elements that are assigned to each lump.

It is further assumed that each sending lump influence can be approximated as a constant value rectangular element patch with the sending cell region determined by the rectangular hull of the elements belonging to the sending lump. The appropriate average displacement discontinuity value in the sending lump is computed from the average values of all elements falling within the lump cell. In order to understand the efficiency of this scheme, define the basic computational cost unit to be the time required to compute the influence of one element or one lump at any receiving point.

If the total problem area is A , and the total number of elements is N , the average element size g is defined in Equation [2] to be equal to $\sqrt{A/N}$. At each lump level, it is assumed that lump stress and displacement component influences are transmitted to p points on each receiving lump that form the nodes of an interpolation grid. (For example, $p = 9$ or $p = 16$ for bi-quadratic and bi-cubic interpolations, respectively). The stress and displacement values are then accumulated at the collocation points of each element that is assigned to the receiving lump. The computational effort (or time) of interpolation is assumed to be much smaller than the computational effort associated with the influence evaluation. The lump influences are transmitted to a given receiver lump from all lumps at the same hierarchical level that fall between the boundaries of two square regions defined by an inner 'ring' boundary and an 'outer' ring boundary. The inner ring is centred on the receiving lump and has a side length of $(2s + 1)G_L$ where $s \geq 1$ is the lump gap parameter (see Figure 6). The outer ring is centred on the parent lump containing the receiving lump and has a side length of $2(2s + 1)G_L$. The total number of sending lumps of size G_L between the inner and outer ring boundaries is therefore equal to $3(2s + 1)^2$. The total number of receiving lumps of size G_L is nominally equal to $A/G_L^2 = N(g/G)^2 / 2^{2L-2}$, using Equation [2] and Equation [6]. Hence the computational effort required to compute the lump influence at p interpolation points at level L is given by

The computational analysis of shallow depth tabular mining problems

$$E_L = 3p(2s+1)^2 N(g/G)^2 / 2^{2L-2} \quad [8]$$

The total effort required to compute the overall lump influence is obtained by summing Equation [8] over all lump levels, $L = 1$ to M . This effectively amounts to summing the geometric progression with terms 2^{2-2L} which has an upper bound equal to $4/3$ when M is large. The maximum computational effort for the lump influence evaluation is therefore not greater than

$$E_M \sim 4p(2s+1)^2 N(g/G)^2 \quad [9]$$

In addition to the lump to lump computations, it is necessary to estimate the computational effort that is required to evaluate the direct influence of all sending elements within the inner ring surrounding each fine level lump. The direct element influences must be evaluated at each collocation point within the elements contained in each fine level lump. If there are c collocation points per element, the number of required receiving influences in each fine lump is equal to $c(G/g)^2$ and the number of sending elements in the inner ring is equal to $(2s+1)^2 (G/g)^2$. Hence the direct influence computational effort, E_D , for all fine level receiving lumps is

$$E_D = (A/G^2)c(2s+1)^2 (G/g)^4 = cN(2s+1)^2 (G/g)^2 \quad [10]$$

Combining Equations [9] and [10], the total computational effort is estimated to be

$$E = N(2s+1)^2 [c(G/g)^2 + 4p(g/G)^2] \quad [11]$$

Several important properties of Equation [11] should be noted. The most striking is that the total computational effort that is required to compute all influence values in a given iteration cycle is proportional to the total number of elements, N . This is significantly better than the effort that would be required for the direct influence transmission between all elements which is proportional to N^2 . The N -proportional property is also marginally better than the performance of an FFT algorithm which is proportional to $N \log N$.

Examination of Equation [11] also implies that the computational effort can be optimized by choosing an appropriate ratio of G/g and by making the factor $(2s+1)^2$ as small as possible. In fact, it is possible to choose $s = 1$ provided the ratio G/g is not too small ($G/g \sim 4$ to 5 is usually satisfactory in this case) and by implementing a high order receiving grid interpolation strategy.

As an illustration of the error behaviour of the interpolation lumping scheme, consider the lumped solution of the circular opening shown in Figure 2 with the fine level (level 1) lump grid size, G , equal to 4 m. Since the average element size is $g \sim 1.17$, the lump:element size ratio is $G/g \sim 3.41$. It is also assumed that in this case the maximum number of allowed lump levels is 2 and the lump gap parameter is $s = 1$.

Figure 7 is a plot of the errors in the normal closure component (designated as DDZ in Figure 7) that arise when no interpolation on the receiving lump grids is performed, compared to the errors arising when bi-quadratic receiving lump influence interpolation is used (parameter $p = 9$). The

'error' is computed relative to the solution that is determined without lumping (see Figure 3) and not relative to the analytical solution. It is clear that the errors are reduced significantly (to lower than 1% relative to the solution with no lumping) when receiving grid interpolation is used. The sending lump structure in these cases is assumed to be a simple rectangular element with a constant value of the displacement discontinuity (DD) vector equal to the average of all DD values in the elements belonging to each sending lump. The sending lump shape is assumed to be the rectangular hull surrounding the sending lump elements in the local element plane.

Additional improvements to the basic lumping scheme, with receiving grid interpolation, may be considered. One possible improvement is to increase the receiving grid interpolation order from bi-quadratic ($p = 9$) to bi-cubic ($p = 16$). It is also found to be beneficial to increase the discontinuity variation order in the sending lumps at the finest lump level (level 1). This may be increased to maximum effect by using direct influence transmission from the individual elements comprising the sending lumps at the finest lump level.

To illustrate these possibilities consider the following four cases; (a) Bi-quadratic (9 node) receiving lump grid interpolation and constant rectangular sending lump structure; (b) Bi-cubic (16 node) receiving lump grid interpolation and constant rectangular sending lump structure; (c) Bi-quadratic (9 node) receiving lump grid interpolation and direct element influence transmission from level 1 sending lumps; (d) Bi-cubic (16 node) receiving lump grid interpolation and direct element influence transmission from level 1 sending lumps. The error values of the normal closure component (designated as DDZ) for these four cases are illustrated in Figure 8. (The error is again computed relative to the solution values that are obtained without lumping). The two cases (a) and (b) where constant rectangular lump sending structure is employed are designated by the letter 'R' and the two cases (c) and (d) employing the element-driven sending structure are designated by the letter 'E' in the legend in Figure 8. It is clear that the revised element-driven lumping ('E' type lumping) at level 1 reduces the error levels remarkably to about 0.2% when compared to the solution with no lumping. The use of bi-cubic receiving grid interpolation appears to be most beneficial in combination with the element-driven lump sending scheme (case (d)). Further improvements may be effected (for example, it appears from Figure 8 that the bi-quadratic and bi-cubic interpolation could be averaged to reduce the error bias) but these improvements are arguably irrelevant in relation to the excellent performance of the combined bi-cubic interpolation and E-type sending combination.

The lumping scheme improvements that have been discussed here have concentrated mainly on describing strategies to improve the error properties of lumping. In the particular case of the circular excavation example illustrated in Figure 2, the run times are reduced to about 40% of the run time arising without lumping. However, for the solution of large-scale problems, comprising 10 000 to 100 000 or more collocation points, it is infeasible to carry out the

The computational analysis of shallow depth tabular mining problems

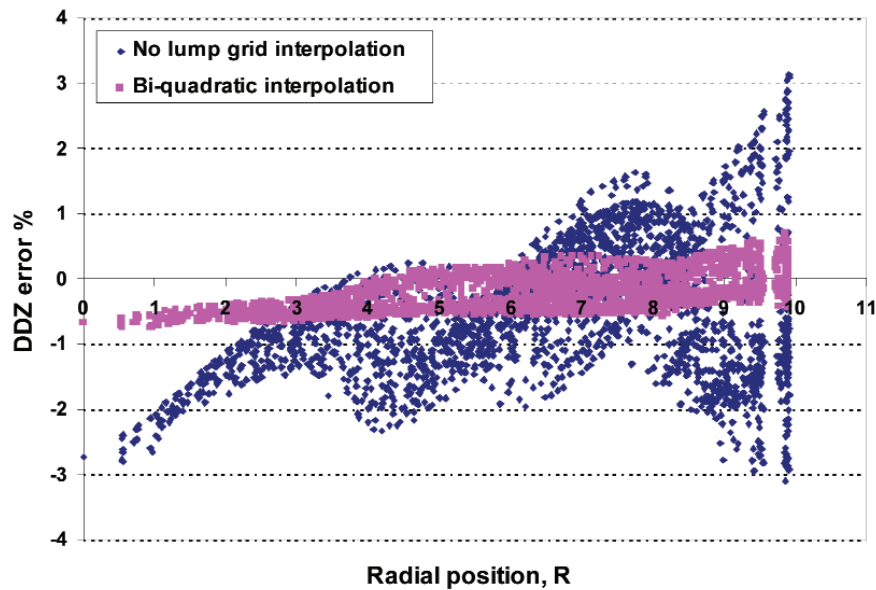


Figure 7—Effect of receiving lump grid interpolation in reducing the error in the normal closure component, DDZ, in a circular excavation relative to the values estimated with no lumping

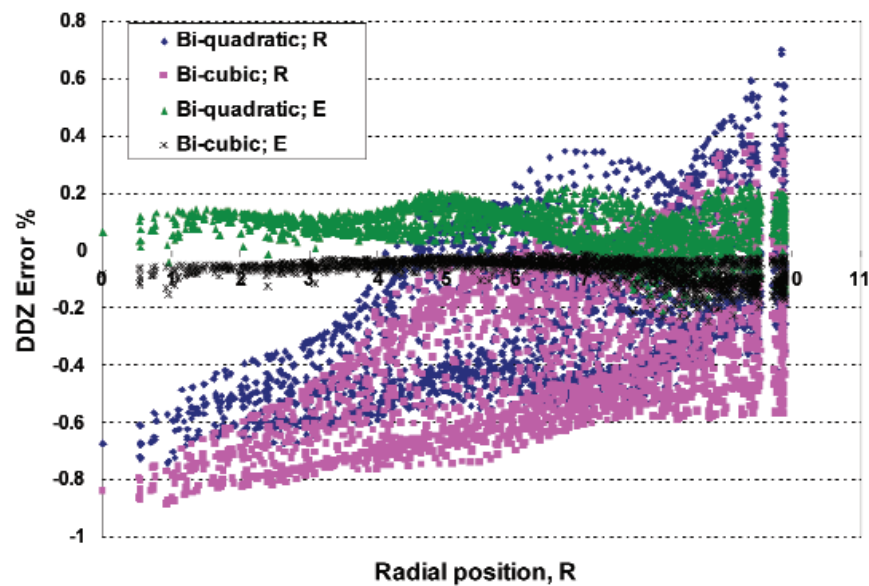


Figure 8—Comparison of errors arising from different lumping strategies, in terms of the error in the normal closure component, DDZ, relative to the values estimated with no lumping. (The symbol 'R' in the legend designates sending lumps approximated as rectangular elements with constant average displacement discontinuity values. The symbol 'E' designates sending from individual elements at lump level 1)

solution without the implementation of a lumping scheme. It should be noted, as well, that the scheme outlined here is designed to solve the interactive movements on multiple reef planes, at arbitrary orientations, as well as the potential intersection of fault planes with reef planes.

Pillar and face edge failure models

In the design of platinum mine layouts, a large number of small in-stope pillars are typically used next to the gullies. These pillars are required to provide the necessary support resistance to prevent massive collapses caused by the

presence of large tensile regions in the hangingwall. In the very shallow areas, bord and pillar mining methods are also used in the platinum industry. Explicitly simulating a large number of these small pillars using uniform, square-shaped displacement discontinuity elements associated with traditional DDM codes, is not practical. The use of the partially mined element strategy developed in the MINSIM-D code (Ryder and Napier, 1985) precludes the direct estimation of the actual load carried by the pillars — one of the primary unknowns in a pillar mining analysis. It also becomes difficult to estimate local strata stiffness and the stability of irregular shaped pillar structures.

The computational analysis of shallow depth tabular mining problems

A further requirement in the analysis of pillar design problems is to simulate crush pillar behaviour to assess the potential for uncontrolled pillar failures (Van der Merwe, 2006, Watson *et al.*, 2007) and the possibility of the possible violent 'bursting' of over-sized crush pillars or pillar remnants. The simulation of such failures is computationally challenging and, in general, requires the application of some form of nonlinear finite element or distinct element model. The integration of such models with the displacement discontinuity tabular model is not straightforward.

If the fractured seam or reef material is known to be concentrated within or close to the mining horizon and does not extend appreciably into the hangingwall or footwall regions, as will often be the case when considering the design of crush pillars in shallow pillar mining layouts, it is possible to assume that the material close to the pillar or face edge is in a semi-fractured 'limit equilibrium' state (see, Brummer, 1987 and Malan and Napier, 2006). A vertical cross-section through the assumed fractured region, bounded by the excavation roof and floor, is depicted in Figure 9.

Since the material at the stope face is free-standing, it is assumed that the limiting failure state is controlled by a relationship of the form

$$\sigma_n(x) = C + m\sigma_s(x) \quad [12]$$

where x is the distance, in the plane of the excavation, into the fractured region, normal to the stope face. $\sigma_n(x)$ is the average stress component normal to the plane of the seam or reef horizon at position x , and $\sigma_s(x)$ represents the seam-parallel (or reef-parallel) stress averaged over the mining height, H , of the seam region. Parameter C is a cohesion term, required to allow the free-standing face condition $\sigma_n(0) > 0$ if $\sigma_s(0) = 0$ and m is related to the sliding friction of the fractured material.

Local equilibrium of an incremental section of the fractured material between positions x and $x + \Delta x$, and for a unit distance out of the plane of Figure 9, is maintained if the following relationship is satisfied.

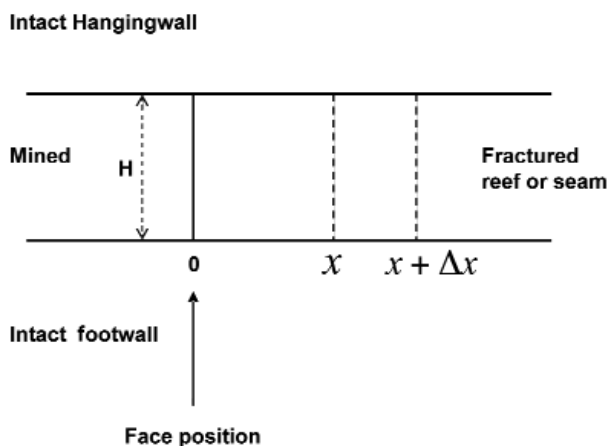


Figure 9. Vertical section, through the stope face and in direction, x , normal to the stope face, that is used to compute average reef or seam stress components in the assumed fractured region

$$H\sigma_s(x + \Delta x) = H\sigma_s(x) + 2\tau(x)\Delta x \quad [13]$$

In Equation [13], $\tau(x)$ is an equilibrating shear stress that acts at the interface between the fractured material and the intact hangingwall and footwall regions. Assume that the shear stress, $\tau(x)$, is related to the reef-normal stress component, $\sigma_n(x)$ according to a friction sliding condition of the form

$$\tau(x) = \tan \phi_s \sigma_n(x) = \mu_s \sigma_n(x) \quad [14]$$

where ϕ_s is the effective interface friction angle (with corresponding friction coefficient, $\mu_s = \tan \phi_s$). Taking the limit $\Delta x \rightarrow 0$, in Equation [13] and employing the limit equilibrium condition given by Equation [12], yields the differential equation

$$\frac{d\sigma_s}{dx} = \frac{2\mu_s}{H} (C + m\sigma_s) \quad [15]$$

Assuming the boundary condition $\sigma_s(0) = 0$, Equation [15] has the solution

$$\sigma_s(x) = C(e^{\alpha x} - 1)/m \quad [16]$$

where $\alpha = 2\mu_s m / H$ [17]

Substituting Equation [16] into Equation [12] yields the companion expression for $\sigma_n(x)$.

$$\sigma_n(x) = Ce^{\alpha x} \quad [18]$$

The critical assumption is made that Equations [16] and [18] can be applied directly to the case of complex pillar and face outlines, by interpreting the distance x as the minimum distance from any point within the reef-plane projection of the solid pillar region or abutment region to the face edge polygon bounding the region. For tabular mine layout geometries, it is straightforward to compute this distance for all pillar and abutment element collocation points. This simple approach then permits the limit equilibrium model to be applied to general tabular layout problems with irregular shaped pillars. Naturally, the procedure suggested here represents an extreme simplification of the true three-dimensional, nonlinear failure processes arising in the vicinity of excavation edges, but is compatible with the approximations made in assuming a displacement discontinuity representation of the mining excavation. The detailed limitations of this approach have to be evaluated against more detailed failure models and, importantly, against the results of direct field observations.

Equations [16] and [18] will apply only up to a critical distance, $x = L$, from the edge of the pillar, at which point it is assumed that the normal stress, $\sigma_n(x)$, is insufficient to cause failure. This transition state is assumed to be controlled by a failure condition of the form

$$\sigma_n = C_0 + m_0\sigma_s \quad [19]$$

where C_0 and m_0 are the intact material strength parameters. In addition, the intact seam or reef material may be assumed to deform according to a linear stiffness response given by

$$\sigma_n = \sigma_n^P + kD_n \quad [20]$$

The computational analysis of shallow depth tabular mining problems

where σ_n^p is the primitive stress component normal to the reef plane at the point of interest, D_n is the difference in the normal displacement component between the roof and floor horizon, and k is a reef or seam stiffness modulus (see, for example, Crouch and Starfield, 1983).

In summary, the proposed limit equilibrium model provides a simple strategy to allow inter-element interaction through the implicit geometric connection between neighbouring elements, as determined by the minimum edge distance, x . The model also allows 'strain softening' for the simulation of pillar crushing or bursting, when the parameters C_0 and m_0 exceed the residual values of C and m respectively. It is important to note that this model is not equivalent to any model based on the specification of limiting peak and residual stress values that are applied locally at all points of the pillar regions or edge abutments.

Consider, for example, the case of a horizontal, parallel-sided panel of span 50 m in a rock mass having the properties summarized in Table I. Figure 10 illustrates the simulated excavation closure and stress state, relative to the right hand edge of the panel, exhibiting a peak stress in the solid region ahead of the stope face.

Shallow depth and multiple reef problems

The evaluation of stress distributions in shallow pillar mining problems presents a considerable computational challenge. Shallow conditions can be simulated by erecting an artificial 'excavation' at the surface horizon and including this in the interactive solution of other 'real' underground mining excavations. This approach may require long run times and requires some decision relating to the appropriate truncation of the surface 'excavation' extent. In certain instances, the grid sizes of the surface plane may preclude the close approach of underground reef planes and may lead to iterative solution difficulties. Alternatively, it is possible to develop appropriate influence functions that allow for the

effect of the stress-free surface to be included automatically without requiring the explicit surface plane solution. These shallow depth influence functions are seldom published for three-dimensional displacement discontinuity elements and are currently not implemented in any tabular excavation analysis codes using higher order elements, in South Africa. For completeness and for reference, a simplified derivation of the shallow depth influence function expressions is given in Appendix A.

The shallow depth, higher order, flexible element shape approach presented here has been implemented in a computer code called TEXAN (an acronym standing for Tabular EXcavation ANalysis code). An illustrative example of the application of the TEXAN code is the proposed strike extension of mining panels on the UG2 reef, below previously mined portions of the Merensky reef (see Malan and Napier, 2006). Mining depths are nominally of the order of 60 m to 120 m. Three proposed mining steps, (1), (2) and (3), on the UG2 reef are illustrated in Figure 11, together with the superimposed outline of the previous mining on the overlying Merensky reef plane. The mine outlines are reef plane

Table I

Illustrative parameters used for a limit equilibrium model of face edge failure

Parameter	Value
Intact rock modulus	72 000 MPa
Intact rock Poisson's ratio	0.2
Cohesion, C_0	40 MPa
Slope parameter, m_0	4
Residual cohesion, C	1 MPa
Residual slope parameter, m	2
Seam interface friction angle, ϕ_s	30°
Mining height, H	1.5 m
Seam stiffness modulus, k	40 000 MPa / m

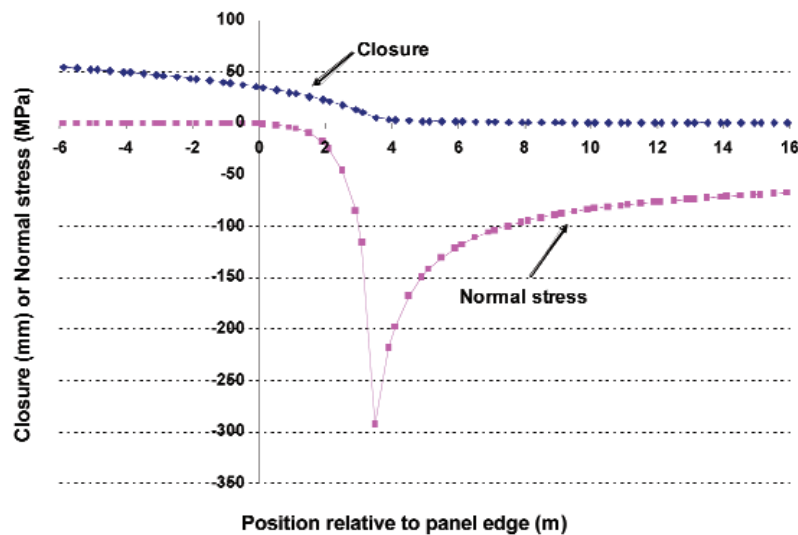


Figure 10—Closure and normal stress relative to the edge position of a parallel-sided panel for a limit equilibrium model of failure ahead of the panel face (positive position values)

The computational analysis of shallow depth tabular mining problems

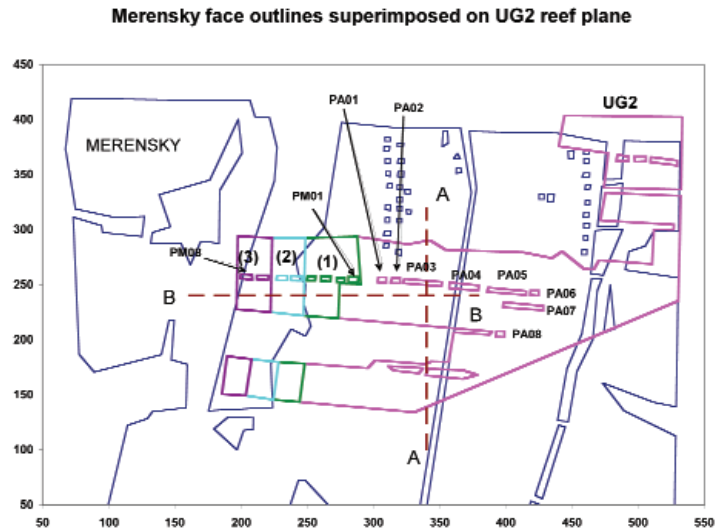


Figure 11—Proposed mining step increments (1), (2) and (3) on the UG2 reef plane underlying a previously mined region of the Merensky reef. Note that mining steps 2 and 3 will undermine the Merensky remnant

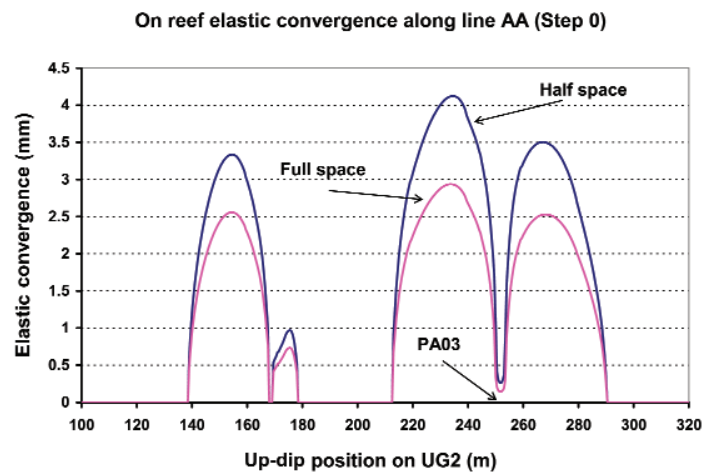


Figure 12—Normal component of elastic convergence along up-dip line AA on the UG2 reef plane (see Figure 11), comparing results for full-space and half-space influence functions

projections and the reef-normal separation distance between the reef planes is approximately 33.4 m. Eight pre-existing pillars on the UG2 reef are highlighted in Figure 11 and are labelled PA01, PA02, PA03, PA04, PA05, PA06, PA07 and PA08 respectively. Eight additional pillars are to be formed in the extended mining blocks on the UG2 reef. These are designated as PM01 through to PM08 (only pillars PM01 and PM08 are explicitly labelled in Figure 11). Pillars PM01, PM02, PM03 and PM04 are formed during the extraction of mining step 1. Pillars PM05 and PM06 are formed in mining step 2, and pillars PM07 and PM08 are formed in mining step 3. The main objective of the simulation is to determine the average pillar stresses arising in each extraction step and, in particular, to note whether any pillar failures occur. The pillar behaviour is described using the crush model parameters given in Table I. However, the intact rock modulus and Poisson's ratio was set to 68 000 MPa and 0.3 respectively, with the in-seam stiffness modulus, k , set

to 61025.6 MPa/m. The vertical and horizontal primitive stress gradients were assumed to be equal to 0.032 MPa/m and 0.048 MPa/m respectively. The lines marked AA and BB in Figure 11 represent dip and strike lines, respectively where certain field points are evaluated. An important feature to note in Figure 11 is that the extraction of mining steps (2) and (3) occurs under an unmined region of the superimposed Merensky reef plane.

An indication of the difference between the layout behaviour when using full-space or half-space influence functions (also referred to as the 'infinite' or 'shallow' depth influence kernels) can be difficult to judge when considering multi-reef problems. Consider, for example, the state of the mining layout prior to the extraction of the mining step increments, designated as Step 0. Figure 12 shows a plot of the normal component of elastic convergence along the strike line AA (see Figure 11) and Figure 13 is a corresponding plot of the reef-normal stress component computed 0.2 m above

The computational analysis of shallow depth tabular mining problems

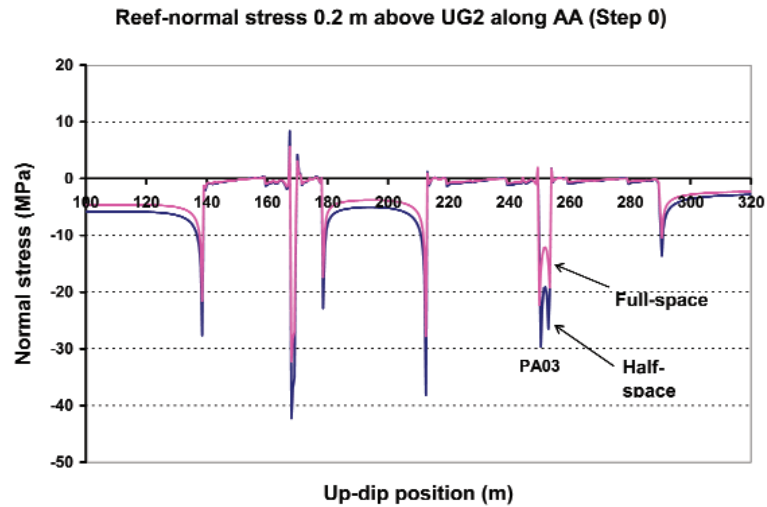


Figure 13—Normal component of stress 0.2 m above the excavation surface and parallel to the up-dip line AA on the UG2 reef plane (see Figure 10), comparing results for full-space and half-space influence functions

the UG2 reef plane. The closure levels are small (in general agreement with underground observations) but appear to be somewhat larger when the analysis is carried out using the shallow depth (half-space) influence kernels. Although the pillar PA03 is over-mined, it must be noted that the active span on the UG2 reef plane along the line AA is of the order of 100 m, leading to significant levels of stress being carried by the narrow mid-span pillar PA03, as shown in Figure 13. Figure 13 also suggests that the stress in the pillar PA03 is greater when the analysis is carried out with the half-space influence functions than with the full-space influence functions. This conclusion is, however, misleading when the average stress values over the entire pillar area are computed. It is found, in fact, that in Step 0 the average stress in pillar PA03 is 19.92 MPa when using the full-space influence kernels, compared to an average value of 18.80 MPa computed using half-space influence kernels. The apparent discrepancy suggested by Figure 13 arises from the fact that the detailed stress distribution across the pillar strike dimension is significantly different in each case.

Table II presents a summary of the average pillar stress values that arise in pillars PA01 to PA08 in mining Step 0, Step 1, Step 2 and Step 3, respectively, when using full-space ('infinite' depth) influence functions. Table III is a summary of the corresponding stress values that arise in the pillars PM01 to PM08 that are formed during the incremental mining process. (See Figure 11 for the pillar numbering). The stress values associated with the pillars PM01 to PM08 in Table III must be interpreted as the average value arising in the position that the pillar occupies within the abutment or the exposed pillar region, depending on the mining step number. It appears from the values given in Table II that the initial pillar series (PA01 to PA08) remain intact following the three mining step increments.

From Table III, it can be seen that the behaviour of the pillars that are exposed following the mining step increments is more complicated. In particular, it can be seen that some pillars are formed initially without failing, whereas others are

formed in a failed state. For example, pillar PM06 is formed without failure in Step 2 but then fails during the mining of Step 3. Pillar PM07 is formed in a failed state in Step 3. From this analysis, and based on the hypothetical pillar strength parameters, it appears that several of the pillars might be prone to 'bursting' after their initial formation.

Table II

Average pillar stress values in pillars PA01 to PA08 as a function of mining step number (full-space influence functions)

Pillar	Step 0	Step 1	Step 2	Step 3
PA01	21.76	22.00	22.02	22.03
PA02	17.23	17.42	17.46	17.49
PA03	19.92	20.07	20.16	20.24
PA04	16.61	17.40	17.76	18.15
PA05	14.98	17.43	18.60	19.86
PA06	14.28	18.86	19.55	20.79
PA07	17.75	17.96	17.98	18.00
PA08	20.30	20.56	20.69	20.62

Table III

Average pillar stress values in formed pillars PM01 to PM08 as a function of mining step number (full-space influence functions)

Pillar	Step 0	Step 1	Step 2	Step 3
PM01	3.94	16.96*	21.50	19.03
PM02	2.77	19.52*	21.04	4.55
PM03	2.77	19.17*	13.52	5.92
PM04	3.52	17.10*	5.07	4.67
PM05	4.21	5.84	5.48*	5.47
PM06	4.54	5.23	17.18*	5.38
PM07	4.23	4.86	7.35	4.93*
PM08	3.91	4.09	4.63	20.57*

*The mining step when the pillar is first formed

The computational analysis of shallow depth tabular mining problems

It is of interest to repeat the mining step analysis using shallow depth (half-space) influence functions. The results are summarized in Tables IV and V and are displayed graphically in Figure 14. It is important to note that in this case more pillars appear to be formed in a residual 'crushed' state than for the case where the 'stiffer' full-space influence functions are used. Obviously, these results are dependent on the particular choice of assumed failure parameters and on the size of the mining step increments of the modelled extraction sequence. However, it would seem that a useful strategy to calibrate the pillar parameters would be to use closure monitoring to quantify pillar deformations and to observe deformation changes before and after pillar failure if possible. Closure profiles along the strike benchmark line BB, shown in Figure 11, are plotted in Figure 15 for the shallow depth analysis. The closure profiles correspond to each mining step. It is interesting to note the increased level of closure for mining step 3, within the strike positions between 200 m to 250 m that fall below an unmined region on the Merensky reef plane. This behaviour was confirmed qualita-

tively by actual on-site measurements of stope closure in this area.

It should be noted that the analyses carried out in this study were performed on a desktop PC having a 2.8 MHz P4 processor. It was found that the pillar softening model required fairly long run times. In the case of the full-space analysis the run time was approximately 7 hours for the four

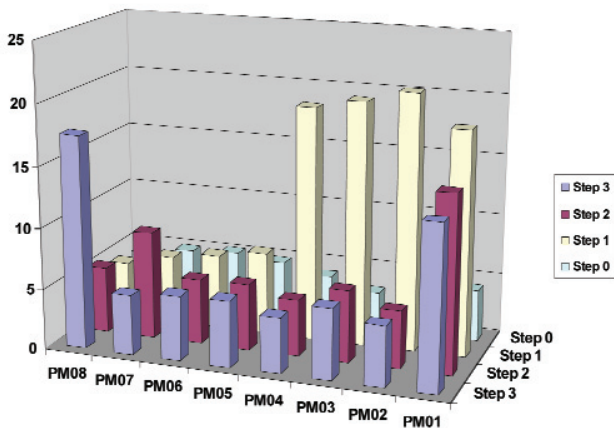


Figure 14—Evolution of average stress values in the pillars PM01 to PM08 formed during mining steps 0 to 3 (half-space influence functions)

Table IV

Average pillar stress values in pillars PA01 to PA08 as a function of mining step number (half-space influence functions)

Pillar	Step 0	Step 1	Step 2	Step 3
PA01	10.43	6.49	6.46	6.54
PA02	20.47	20.39	20.32	19.27
PA03	18.80	18.35	18.45	17.66
PA04	19.44	19.20	19.75	18.11
PA05	18.83	21.08	19.74	19.44
PA06	16.59	20.24	19.20	16.39
PA07	19.42	19.39	19.53	19.17
PA08	17.59	17.79	16.12	13.37

Table V

Average pillar stress values in formed pillars PM01 to PM08 as a function of mining step number (half-space influence functions)

Pillar	Step 0	Step 1	Step 2	Step 3
PM01	4.26	18.43*	14.53	13.37
PM02	2.94	21.02*	4.75	4.96
PM03	3.05	21.05*	5.89	5.84
PM04	4.02	19.28*	4.64	4.59
PM05	4.81	6.81	5.44*	5.42
PM06	5.21	6.16	5.35*	5.34
PM07	4.99	5.64	8.87	4.90*
PM08	4.34	4.67	5.49	17.52*

*The mining step when the pillar is first formed

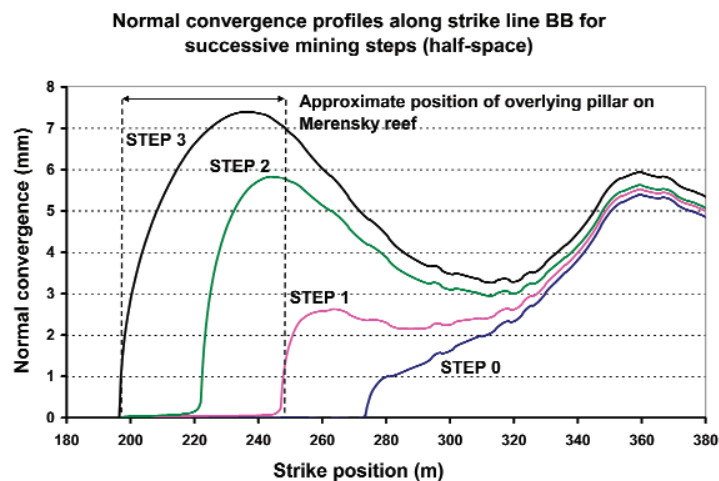


Figure 15—Evolution of normal elastic convergence along strike line BB during successive mining steps on UG2 reef plane with shallow depth influence functions

The computational analysis of shallow depth tabular mining problems

mining steps with a total of 37 154 collocation points in all elements in the model. The run time for the half-space analysis was much slower and required approximately 70 hours. It appears that the long run times are related to the inherent instability of the pillar softening models. However, these run times can be reduced considerably by the use of more sophisticated numerical iteration strategies.

Conclusions

A number of improved computational strategies related to the analysis of shallow depth tabular pillar layouts in a hard rock environment have been presented. These include the incorporation of irregular element shape tessellations with an efficient hierarchical solution scheme that includes the treatment of higher order displacement discontinuity shape variations. This is fully integrated with the ability to treat half-space element influence functions. These improvements are illustrated by the application of the computer analysis to an actual shallow depth pillar layout problem arising in a hard-rock platinum mine. The results depend on ad hoc assumptions that have been made relating to the effective rock modulus, the primitive stress state and the assumed pillar intact and residual strength parameters. It is apparent that the accuracy of near-excavation analyses can be improved considerably by the use of higher order element shape functions. A crush seam model has been described that can permit the realistic solution of actual design problems relating to crush or yield pillar formation. Clearly, detailed calibration data for the pillar model is required.

The computational innovations described in the paper form an encouraging basis for further developments. In particular, it is relatively simple to extend the lumping analysis to treat undulating reef and fault planes and to include multiple material zones. The additional introduction of general off-reef failure simulations and the treatment of fault slip dynamics is more challenging.

References

- BRUMMER, R.K. Modelling the Non-linear Behaviour of Fractured Seams in Deep Gold Mines, *APCOM 87. Proceedings of the Twentieth International Symposium on the Applications of Computers and Mathematics in the Mineral Industries*, vol. 1: Mining, Johannesburg, SAIMM, 1987. pp. 21–32.
- BRADY, B.H.G. and BRAY, J.W. The Boundary Element method for elastic analysis of tabular orebody extraction, assuming complete plane strain. *Int. J. Rock Mech. Min. Sci. & Geomech. Abstr.*, vol. 15, 1978. pp. 29–37.
- CROUCH, S.L. Two-dimensional analysis of near-surface, single-seam extraction. *Int. J. Rock Mech. Min. Sci. & Geomech. Abstr.*, vol. 10, 1973. pp. 85–96.
- CROUCH, S.L. and STARFIELD, A.M. *Boundary Element Methods in Solid Mechanics*. George Allen & Unwin, 1983.
- DEIST, F.H., GEORGIADIS, E., and MORIS, J.P.E. Computer applications in rock mechanics. *Application of Computer Methods in the Mineral Industry, 10th International Symposium*, Johannesburg, 1972.
- JASWON, M.A. and SYMM, G.T. *Integral equation methods in potential theory and elastostatics*. Academic Press, London, 1977.
- JOHNSON, K.L. *Contact Mechanics*. Cambridge University Press, 1985.
- LANDAU, L.D. and LIFSHITZ, E.M. *Theory of Elasticity*, Third Edition, Pergamon Press, 1986.
- MALAN, D.F. and NAPIER, J.A.L. Practical application of the TEXAN code to solve pillar design problems in tabular excavations. *South African National Institute of Rock Engineering Symposium, 2006*, Rustenburg, 2006. pp. 55–74.
- MORIS, J.P.E. and ORAVECZ, K.I. Theoretical background to the development of a computer code for the modelling of seam-like deposits. *Proceedings of the 26th US Symposium on Rock Mechanics*, Rapid City, South Dakota, 1985. pp. 927–936.
- NAPIER, J.A.L. and HILDYARD, M.W. Simulation of fracture growth around openings in highly stressed, brittle rock. *J. S. Afr. Inst. Min. Metall.*, vol. 92, 1992. pp. 159–168.
- NAPIER, J.A.L. Crack edge collocation for the direct computation of stress intensity factors using the displacement discontinuity method. *South African Journal of Science*, vol. 98, 2002. pp. 481–485.
- NAPIER, J.A.L. and STEPHANSEN, S.J. Analysis of Deep-level Mine Design Problems Using the MINSIM-D Boundary Element Program. *APCOM 87. Proceedings of the Twentieth International Symposium on the Applications of Computers and Mathematics in the Mineral Industries, vol. 1: Mining*. Johannesburg, SAIMM, 1987. pp. 3–19.
- PEIRCE, A.P., SPOTTISWOODE, S.M., and NAPIER, J.A.L. The spectral boundary element method: a new window on boundary elements in rock Mechanics. *Int. J. Rock Mech. Min. Sci. & Geomech. Abstr.*, vol. 29, 1992. pp. 379–400.
- PEIRCE, A.P. and NAPIER, J.A.L. A spectral multipole method for efficient solution of large-scale boundary element models in elastostatics. *Int. j. numer. methods eng.*, vol. 38, 1995. pp. 4009–4034.
- PFALZNER, S. and GIBBON, P. *Many-body tree methods in physics*. Cambridge University Press, 1996.
- PLEWMAN, R.P., DEIST, F.H., and ORTLEPP, W.D. The development and application of a digital computer method for the solution of strata control problems. *J. S. Afr. Inst. Min. Metall.*, vol. 70, 1969. pp. 33–44.
- RYDER, J.A. and OFFICER, N.C. An elastic analysis of strata movement observed in the vicinity of inclined excavations. *J. S. Afr. Inst. Min. Metall.*, vol. 64, 1964. pp. 219–244.
- RYDER, J.A. and NAPIER, J.A.L. Error analysis and design of a large-scale tabular mining stress analyser. *5th Int. Conf on Num Methods in Geomech.*, Nagoya, Japan, 1985. pp. 1549–1555.
- SALAMON, M.D.G. Elastic analysis of displacements and stresses induced by the mining of seam or reef deposits—Part I: Fundamental principles and basic solutions as derived from idealised models. *J. S. Afr. Inst. Min. Metall.*, vol. 63, 1963. pp. 128–149. Part II: Practical methods of determining displacement, strain and stress components from a given mining geometry. *J. S. Afr. Inst. Min. Metall.*, vol. 64, 1964. pp. 197–218. Part III: An application of the elastic theory: Protection of surface installations by underground pillars. *J. S. Afr. Inst. Min. Metall.*, vol. 64, 1964. pp. 468–500. Part IV: Inclined reef. *J. S. Afr. Inst. Min. Metall.*, vol. 65, 1965. pp. 319–338.
- SALAMON, M.D.G., BADR, S., MENDOZA, R., and OZBAY, M.U. Pillar Failure in Deep Coal Seams: Numerical Simulation. *Proceedings of the 10th Congress of the International Society for Rock Mechanics*, The South African Institute for Mining and Metallurgy, Johannesburg, 2003. pp. 1011–1018.
- SNEDDON, I.N. *Fourier Transforms*. McGraw-Hill, 1951.
- SPOTTISWOODE, S.M. Keynote address: Synthetic seismicity mimics observed seismicity in deep tabular mines. *5th International Symposium on Rockbursts and Seismicity in Mines* Van Aswegen, G., Durrheim, R.J. and Ortlepp, W.D. (eds), *J. S. Afr. Inst. Min. Metall.*, 2004. pp. 371–378.
- STUART, A.D. An application of the fast Fourier transform in numerical elasticity. M.Sc. Thesis, University of the Witwatersrand, Johannesburg, 1979.
- VAN DER MERWE, J.N. Beyond Coalbrook: what did we really learn? *J. S. Afr. Inst. Min. Metall.*, vol. 106, 2006. pp. 857–868.
- VIJAYAKUMAR, S., YACOB, T.E., and CURRAN, J.H. A node centric indirect boundary element method: Three-dimensional discontinuities. *Int. J. Computers & Structures*, vol. 76, 2000. pp. 687–703.
- WATSON, B.P., ROBERTS, M.K.C., NKWANA, M.M., KUIJPERS, J., and VAN ASWEGEN, L. The stress-strain behaviour of in-stope pillars in the Bushveld Platinum deposits in South Africa. *J. S. Afr. Inst. Min. Metall.*, vol. 107, 2007. pp. 187–194.
- WILES, T.D. Reliability of numerical modelling predictions. *Int. J. Rock Mech. Min. Sci.* vol. 43, 2006. pp. 454–472.
- YACOB, T.E. and CURRAN, J.H. Analysis of post-peak pillar behaviour using the enhanced displacement discontinuity method. *Proceedings of the 37th U.S. Rock Mechanics Symposium*, Balkema, 1999. pp. 169–176.
- ZIFF, R.K. Mulsim-NL Theoretical and Programmer's Manual. BuMines IC 9322, 1992. ◆

The computational analysis of shallow depth tabular mining problems

Appendix A

Derivation of shallow depth, three-dimensional displacement discontinuity influence functions

Consider a point displacement discontinuity vector $D_i(Q)$ located at point $Q(\xi, \eta, \zeta)$ on a discontinuity surface ∂B having a smooth tangent and with normal vector $n_i(Q)$ as shown in Figure A1. Q is assumed to be located in the region $z \geq 0$ and the components of the displacement discontinuity vector are defined to be equal to the jump in the displacement vector $u_i(Q)$ across the discontinuity surface ∂B . Specifically,

$$D_i(Q) = u_i^-(Q) - u_i^+(Q) \quad [A1]$$

where $u_i^+(Q)$ refers to the displacement vector components on the side of the discontinuity corresponding to the positive normal direction, $n_i(Q)$, and $u_i^-(Q)$ refers to the displacement vector components on the opposite side of the discontinuity surface at point Q .

It is required to determine the induced displacement vector and stress tensor components at a general field point P in the region $z \geq 0$ with the condition that the surface, $z = 0$, should be stress free. In order to construct this stress state, define an image point $\hat{Q}(\xi, \eta, -\zeta)$ in the region $z < 0$ and assume that an image discontinuity vector $\hat{D}_i(\hat{Q})$ is defined at point \hat{Q} with respect to an image normal vector $\hat{n}_i(\hat{Q})$.

The components of the image displacement discontinuity and normal vectors are defined in terms of the actual vector components, D_i and n_i , by the relationships:

$$\begin{bmatrix} \hat{D}_x \\ \hat{D}_y \\ \hat{D}_z \end{bmatrix} = \begin{bmatrix} D_x \\ D_y \\ -D_z \end{bmatrix} \quad \text{and} \quad \begin{bmatrix} \hat{n}_x \\ \hat{n}_y \\ \hat{n}_z \end{bmatrix} = \begin{bmatrix} n_x \\ n_y \\ -n_z \end{bmatrix} \quad [A2]$$

The subscripts x, y and z are used to imply that the displacement discontinuity and normal vector components are expressed with respect to the global coordinate system depicted in Figure A1 with the x - y plane corresponding to the free surface. The definition of the image point follows the classical approach to constructing the Green's function for a half-space. The specific choice of components, defined by

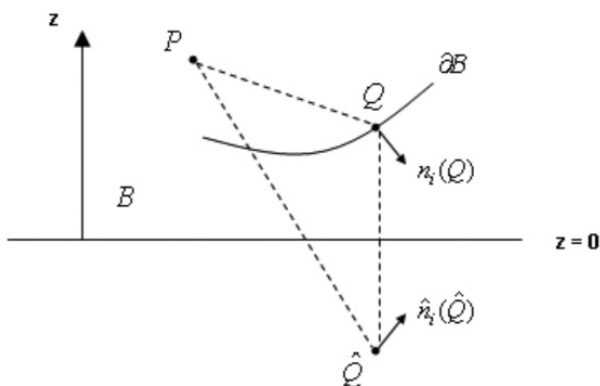


Figure A1—Schematic diagram of a discontinuity surface ∂B in a half-space, B

Equation [A2], ensures that all shear stress components induced by the pair of source points at Q and \hat{Q} will vanish on the surface, $z = 0$. However, the normal stress component $\sigma_{zz}(P_0)$ induced at any point on the surface $z = 0$ will not necessarily vanish and must be compensated by superimposing equal but opposite loads $-\sigma_{zz}(P_0)$ at all points of the surface. This can be accomplished by using the classical Boussinesq solution for a distributed normal load $f(Q_0)$ applied to the planar surface bounding a half-space. This classical solution is expressed in terms of two harmonic potential functions ω and Ω defined by the integral relationships:

$$\omega(P) = \int_S \frac{f(Q_0) dS_{Q_0}}{r} \quad [A3]$$

$$\text{and} \quad \Omega(P) = \int_S f(Q_0) \ln(r+z) dS_{Q_0} \quad [A4]$$

where S designates the surface $z = 0$, $P(x, y, z)$ is a general point in the region $z \geq 0$ and $Q_0(\xi, \eta)$ is a general point on the surface $z = 0$. The distance r in Equations [A3] and [A4] is defined to be

$$r = ((x - \xi)^2 + (y - \eta)^2 + z^2)^{1/2} \quad [A5]$$

From the definitions of ω and Ω it can be seen that

$$\Omega_{,z} = \omega \quad [A6]$$

where the comma notation is used to designate differentiation with respect to a particular independent variable. The displacement vector and stress tensor components induced by the surface load distribution $f(Q_0)$ are given by the following expressions (see, for example, Johnson, 1985).

$$u_x = -(z\omega_{,x} + (1 - 2\nu)\Omega_{,x}) / 4\pi G \quad [A7]$$

$$u_y = -(z\omega_{,y} + (1 - 2\nu)\Omega_{,y}) / 4\pi G \quad [A8]$$

$$u_z = (2(1 - \nu)\omega - z\omega_{,z}) / 4\pi G \quad [A9]$$

$$\sigma_{xx} = (2\nu\omega_{,z} - z\omega_{,xx} - (1 - 2\nu)\Omega_{,xx}) / 2\pi \quad [A10]$$

$$\sigma_{yy} = (2\nu\omega_{,z} - z\omega_{,yy} - (1 - 2\nu)\Omega_{,yy}) / 2\pi \quad [A11]$$

$$\sigma_{zz} = (\omega_{,z} - z\omega_{,zz}) / 2\pi \quad [A12]$$

$$\sigma_{yz} = -z\omega_{,yz} / 2\pi \quad [A13]$$

$$\sigma_{xz} = -z\omega_{,xz} / 2\pi \quad [A14]$$

$$\sigma_{xy} = -(z\omega_{,xy} + (1 - 2\nu)\Omega_{,xy}) / 2\pi \quad [A15]$$

In Equations [A7] to [A15], G is the material shear modulus and ν is Poisson's ratio. In these and subsequent expressions, the 'comma' notation is used to designate differentiation with respect to a specific independent variable or component. Thus $\Omega_{,x} \equiv \partial\Omega/\partial x$ etc. Differentiating Equation [A3] with respect to z , and allowing z to tend to zero, it can be shown that

The computational analysis of shallow depth tabular mining problems

$$\lim_{z \rightarrow 0^+} \left(\frac{\partial \omega}{\partial z} \right) = -2\pi f(P_0) \quad [\text{A16}]$$

with $P_0(x, y)$ being the corresponding point on the surface $z = 0$.

Equation [A16] is the central result that is used to develop a closed form expression for the half-space displacement discontinuity influence function. In particular, if a harmonic function $H(P)$ can be found which has the property that $\partial H / \partial z|_{P=P_0} = f(P_0)$ then it can be inferred that $\omega = -2\pi H$.

Proceeding to the determination of the compensating surface load, it is known that the stress tensor components induced by a displacement discontinuity source vector $D_i(Q)$ within an infinite isotropic elastic region can be determined from the integral representation

$$\sigma_{kl}(P) = \int_{\partial B} \Gamma_{ijkl}(P, Q) D_i(Q) n_j(Q) dS_Q \quad [\text{A17}]$$

evaluated over the discontinuity surface ∂B (see, for example, Jaswon and Symm, 1977). The fundamental influence tensor $\Gamma_{ijkl}(P, Q)$ can be expressed in the form

$$\begin{aligned} \Gamma_{ijkl} = & \frac{G}{4\pi(1-\nu)r^3} \left[(1-4\nu)\delta_{ij}\delta_{kl} - (1-2\nu)(\delta_{ij}\delta_{kl} - \delta_{jk}\delta_{il}) \right. \\ & - 3(1-2\nu)(\delta_{ki}r_jr_l + \delta_{ij}r_kr_l) - 3\nu(\delta_{ik}r_jr_l + \delta_{il}r_jr_k \\ & \left. + \delta_{jk}r_lr_i + \delta_{jl}r_i r_k) + 15r_i r_j r_k r_l \right] \end{aligned} \quad [\text{A18}]$$

In Equation [A18], δ_{ij} represents the Kronecker delta symbol. Implicit summation over repeated subscripts, ranging symbolically over the components x, y, z is assumed. The distance r is equal to $|P - Q|$ and the terms r_i are given by

$$r_x = (x - \xi) / r; \quad r_y = (y - \eta) / r; \quad r_z = (z - \zeta) / r \quad [\text{A19}]$$

For reference, the companion relationships for the displacement components at point P are given by

$$u_k(P) = \int_{\partial B} \Lambda_{ijk}(P, Q) D_i(Q) n_j(Q) dS_Q \quad [\text{A20}]$$

$$\begin{aligned} \text{where } \Lambda_{ijk} = & \frac{1}{8\pi(1-\nu)r^2} \left[(1-2\nu) \right. \\ & \left. (\delta_{ij}r_k - \delta_{ik}r_j - \delta_{jk}r_i) - 3r_i r_j r_k \right] \end{aligned} \quad [\text{A21}]$$

The point contributions to the stress component, $\sigma_{zz}(P_0)$ on the surface $z = 0$, arising from the source and image displacement discontinuity vectors $D_i(Q)$ and $\hat{D}_i(\hat{Q})$, respectively, can be evaluated by expanding the following sums

$$\begin{aligned} \Delta\sigma_{zz}^0(P_0) = & \left[\Gamma_{ijzz}(P_0, Q) D_i(Q) n_j(Q) \right. \\ & \left. + \Gamma_{ijzz}(P_0, \hat{Q}) \hat{D}_i(\hat{Q}) \hat{n}_j(\hat{Q}) \right] \Delta S_Q \end{aligned} \quad [\text{A22}]$$

Using Equations [A2] and carrying out the inner product expansions implied in Equation [A22], it can be shown that

$$\Delta\sigma_{zz}^0(P_0) = \frac{G}{2\pi(1-\nu)r_0^3} \left[F_{ij}(P_0) D_i n_j \right] \Delta S_Q \quad [\text{A23}]$$

where the terms $F_{ij}(x, y)$ are given by

$$\begin{aligned} F_{xx} = & -1 + 4\nu + 3(1-2\nu) \left(\frac{x-\xi}{r_0} \right)^2 \\ & + 3(1-2\nu) \left(\frac{\xi}{r_0} \right)^2 - 15 \left(\frac{x-\xi}{r_0} \right)^2 \left(\frac{\xi}{r_0} \right)^2 \end{aligned} \quad [\text{A24}]$$

$$\begin{aligned} F_{xy} = & 3(1-2\nu) \frac{(x-\xi)(y-\eta)}{r_0^2} \\ & - 15 \frac{(x-\xi)(y-\eta)}{r_0^2} \left(\frac{\xi}{r_0} \right)^2 \end{aligned} \quad [\text{A25}]$$

$$\begin{aligned} F_{xz} = & -3(1-2\nu) \frac{(x-\xi)\xi}{r_0^2} - 6\nu \frac{(x-\xi)\xi}{r_0^2} \\ & + 15 \frac{(x-\xi)}{r_0} \left(\frac{\xi}{r_0} \right)^3 \end{aligned} \quad [\text{A26}]$$

$$F_{yx} = F_{xy} \quad [\text{A27}]$$

$$\begin{aligned} F_{yy} = & -1 + 4\nu + 3(1-2\nu) \left(\frac{y-\eta}{r_0} \right)^2 \\ & + 3(1-2\nu) \left(\frac{\xi}{r_0} \right)^2 - 15 \left(\frac{y-\eta}{r_0} \right)^2 \left(\frac{\xi}{r_0} \right)^2 \end{aligned} \quad [\text{A28}]$$

$$\begin{aligned} F_{yz} = & -3(1-2\nu) \frac{(y-\eta)\xi}{r_0^2} - 6\nu \frac{(y-\eta)\xi}{r_0^2} \\ & + 15 \frac{(y-\eta)}{r_0} \left(\frac{\xi}{r_0} \right)^3 \end{aligned} \quad [\text{A29}]$$

$$F_{zx} = F_{xz} \quad [\text{A30}]$$

$$F_{zy} = F_{yz} \quad [\text{A31}]$$

$$F_{zz} = 1 + 6 \left(\frac{\xi}{r_0} \right)^2 - 15 \left(\frac{\xi}{r_0} \right)^4 \quad [\text{A32}]$$

and where

$$r_0^2 = (x - \xi)^2 + (y - \eta)^2 + \zeta^2 \quad [\text{A33}]$$

It can be demonstrated that each of the terms $F_{ij}(x, y)$ can be matched to full-space functions $F_{ij}^1(x, y, z)$, evaluated at $z = 0$, that can be written in terms of the derivatives of the harmonic function

$$\hat{\phi} = 1 / \hat{r} \quad [\text{A34}]$$

$$\text{where } \hat{r}^2 = (x - \xi)^2 + (y - \eta)^2 + (z + \zeta)^2 \quad [\text{A35}]$$

The details of performing this tedious process for each component, F_{ij} , will not be displayed explicitly but can be carried out by considering all derivatives of $\hat{\phi}$ up to third

The computational analysis of shallow depth tabular mining problems

order and substituting these, by inspection, into Equations [A24] to [A32]. For example, it can be shown that Equation [A24] for $F_{xx}(x,y)$ can be matched to the expression $F'_{xx}(x,y,z)$ which has the form:

$$F'_{xx}(x,y,z) = -2\nu \frac{\partial^2}{\partial z^2} \left(\frac{1}{\hat{r}} \right) + (1-2\nu) \frac{\partial^2}{\partial x^2} \left(\frac{1}{\hat{r}} \right) + \zeta \frac{\partial^3}{\partial x^2 \partial z} \left(\frac{1}{\hat{r}} \right) \quad [A36]$$

and which has the property that $F'_{xx}(x,y,0) = F_{xx}(x,y)$. Since $\partial \ln(\hat{r} + z + \zeta) / \partial z = \hat{\phi}$, Equation [A36] can be written, in turn, as a partial derivative function with respect to z as follows.

$$F'_{xx} = \partial / \partial z \left\{ -2\nu \frac{\partial}{\partial z} \left(\frac{1}{\hat{r}} \right) + (1-2\nu) \frac{\partial^2}{\partial x^2} \ln(\hat{r} + z + \zeta) + \zeta \frac{\partial^2}{\partial x^2} \left(\frac{1}{\hat{r}} \right) \right\} \quad [A37]$$

The expression in curly brackets in Equation [A37] therefore represents an appropriate harmonic function H_{xx} that can be employed to assemble the overall function ω used in Equations [A7] to [A15]. It is necessary also to integrate the functions H_{ij} with respect to z in order to define the contributing terms that are used to express the function Ω in Equations [A7] to [A15]. These steps can be facilitated by defining the harmonic functions

$$\hat{\theta} = (z + \zeta) \ln(\hat{r} + z + \zeta) - \hat{r} \quad [A38]$$

$$\text{and } \hat{\chi} = \ln(\hat{r} + z + \zeta) \quad [A39]$$

From the definitions [A38] and [A39], it can be shown that $\hat{\chi} = \partial \hat{\theta} / \partial z$ and $\hat{\phi} = \partial \hat{\chi} / \partial z$. Hence, the overall potential function Ω , for the compensating surface load, can be expressed as the sum

$$\Omega = \hat{\Omega}_{ij} D_i n_j \quad [A40]$$

where the individual terms $\hat{\Omega}_{ij}$ are symmetric in i and j (following the symmetry of the functions $F_{ij} = F_{ji}$, defined by Equations [A24] to [A32]) and are given by

$$\hat{\Omega}_{xx} = \frac{G}{(1-\nu)} (-2\nu \hat{\phi} + (1-2\nu) \hat{\theta}_{,xx} + \zeta \hat{\chi}_{,xx}) \quad [A41]$$

$$\hat{\Omega}_{yy} = \frac{G}{(1-\nu)} (-2\nu \hat{\phi} + (1-2\nu) \hat{\theta}_{,yy} + \zeta \hat{\chi}_{,yy}) \quad [A42]$$

$$\hat{\Omega}_{zz} = \frac{G}{(1-\nu)} (-\hat{\phi} + \zeta \hat{\chi}_{,z}) \quad [A43]$$

$$\hat{\Omega}_{yz} = -\frac{G}{(1-\nu)} \zeta \hat{\phi}_{,y} \quad [A44]$$

$$\hat{\Omega}_{xz} = -\frac{G}{(1-\nu)} \zeta \hat{\phi}_{,x} \quad [A45]$$

$$\hat{\Omega}_{xy} = \frac{G}{(1-\nu)} ((1-2\nu) \hat{\theta}_{,xy} + \zeta \hat{\chi}_{,xy}) \quad [A46]$$

Expressions for the overall potential function ω , corresponding to Ω (Equations [A40]), are obtained from the relationship

$$\omega = \partial \Omega / \partial z \quad [A47]$$

Substituting the functions ω and Ω into Equations [A7] to [A15] allows the final expression for the compensating surface load to be written in a closed analytic form.

Appendix B

High order polynomial shape function formulation

Polynomial shape functions, for triangular and quadrilateral elements, can be derived easily when the element collocation points are arranged on intersecting straight lines (as in Figures 1a and 1b). In these cases, the overall DD variation, $V_i(x,y)$ of each DD component i can be expressed in terms of the sum

$$V_i(x,y) = \sum_{j=1}^N D_{ij} \psi_j(x,y) \quad [B1]$$

where the sum is evaluated over all collocation points $j = 1$ to $j = N$ in the element and D_{ij} represents the value of component i of the displacement discontinuity vector at collocation point j . The so-called 'shape' functions, $\psi_j(x,y)$, are all n^{th} , or lower, order polynomials and depend only on the collocation point positions and have the property that shape function j is zero at all collocation points except at collocation point j where it is equal to unity. Specifically,

$$\psi_j(x_k, y_k) = \delta_{jk} \quad [B2]$$

where δ_j is the Kronecker delta symbol with values $\delta_{jk} = 1$ if $j = k$ and $\delta_{jk} = 0$ if $j \neq k$. The shape functions should also have the property that for any point x, y

$$\sum_{j=1}^N \psi_j(x,y) = 1 \quad [B3]$$

Each n^{th} order shape function can be assembled from product functions of the form

$$W_j(x,y) = \prod_{k=1}^n \lambda_{jk}(x,y) \quad [B4]$$

in which λ_{jk} represents straight lines passing through selected sets of the collocation points. The functions λ_{jk} corresponding to each line k assume the functional form

$$\lambda_{jk}(x,y) = a_{jk}x + b_{jk}y + c_{jk} \quad [B5]$$

The coefficients a_{jk} , b_{jk} and c_{jk} are such that $\lambda_{jk} = 0$ when any point x, y falls on line k and are also chosen to satisfy the condition that $\lambda_{jk}(x_j, y_j) = 1$ at point j . For example, the product of the three lines passing through the collinear points parallel to each side of the triangular element in Figure 1a would be used to assemble the product function for the centre point in Figure 1a, using Equations [B4] and [B5]. Although the coefficients a_{jk} , b_{jk} and c_{jk} can be chosen to satisfy the condition $W_j(x_k, y_k) = \delta_{jk}$, functions $W_j(x,y)$ will not, in

The computational analysis of shallow depth tabular mining problems

general, satisfy the condition given by Equation [B3]. However, Equation [B3] can be satisfied by defining the modified function

$$\psi_j(x, y) = W_j(x, y) + (1 - S_N(x, y)) / N \quad [B6]$$

where

$$S_N(x, y) = \sum_{j=1}^N W_j(x, y) \quad [B7]$$

The transformation defined by Equation [B6] is required to develop shape functions for general quadrilateral elements such as the particular example depicted in Figure 1b.

Stress and displacement influence functions, based on polynomial functions of the form given by Equation [B1], can be evaluated conveniently at a specified space point, x_P, y_P, z_P , defined with respect to the element plane coordinate system, by using the polar coordinate transformation $x = x_P + \rho \cos \theta, y = y_P + \rho \sin \theta, z = z_P$. Substituting these expressions into Equation [A18], the required influence coefficients can be determined by evaluating basic integrals of the form

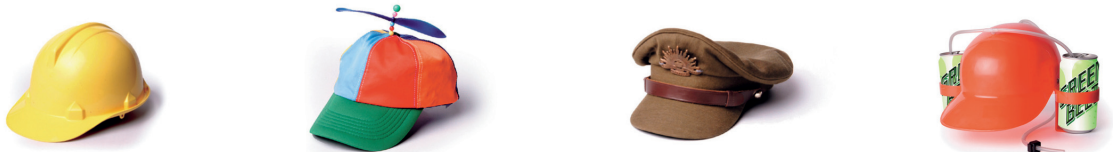
$$I_{pq}(k, m; z) = \int \sin^p \theta \cos^q \theta \left\{ \int_0^{R(\theta)} \frac{\rho^{k+1} d\rho}{(\rho^2 + z^2)^{m/2}} \right\} d\theta \quad [B8]$$

where k and m are integers that assume the values $0 \leq k \leq n$ and $m = 3, 5$ or 7 . The limit $R(\theta)$ in Equation [B8] is the distance from the in-plane receiving point projection coordinates x_P, y_P to a particular point on the boundary of the element. The outer integral in Equation [B8] is understood to imply a complete circuit around the perimeter of the element. In the case when x_P, y_P falls within the element boundary and $z = 0$, special care has to be exercised to interpret the lower limit of the inner integral in terms of the Hadamard finite part concept. (See, for example, Napier, 2002). For polynomial variations of the DD vector, such as in Equation [B1], the inner integral in Equation [B8] can be evaluated analytically. The outer integral can be evaluated analytically, or numerically, depending on the detailed shape of the element boundary. ♦



GEOTECHNICAL ENGINEERING RESOURCE EVALUATION CORPORATE SERVICES TRAINING & MENTORING EXPLORATION PROJECT MANAGEMENT

The many hats of Snowden



MINING ENGINEERING INFORMATION TECHNOLOGY PROJECT MANAGEMENT BUSINESS IMPROVEMENT

Snowden provides a comprehensive range of consulting services and independent advice to exploration and mining companies, as well as financial and legal institutions with interests in the mining sector.

SNOWDEN

www.snowdengroup.com

JOHANNESBURG +27 11 782 2379 PERTH +61 8 9213 9213 BRISBANE +61 7 3231 3800 VANCOUVER +1 604 683 7645 LONDON +44 1932 268701 BELO HORIZONTE +55 31 3222 6286